ACS OMEGA

http://pubs.acs.org/journal/acsodf

Article

3D Printed Gas Distributor for Enhanced Production of $CaCO_3$ via Bubbling Carbonation

Kai-li Wu, Xiang Li, Zhong-xing Xu, and Chang-jun Liu*

Cite This: *ACS Omega* 2023, 8, 2398−2405

Read Online

ACCESS | Metrics & More | Article Recommendations | Supporting Information

ABSTRACT: Bubbling carbonation is the most widely used method for production of $CaCO_3$. A structure-controllable preparation of calcium carbonate with homogeneous crystallinity and narrow particle size distribution is generally required. In this work, a gas distributor is designed and fabricated by light-curing three-dimensional (3D) printing technology to optimize the pore size and distribution of the distributor. The printed gas distributor is combined with a home-made glass vessel to form a simple carbonation reactor without the need for stirring. With the optimized gas flow rate and concentration of $Ca(OH)_2$, this reactor produces small-sized bubbles continuously and uniformly. A homogeneous bubble flow regime can be thus easily formed with the printed distributor, which leads to an enhanced production of calcium carbonate at room temperature with a uniform morphology and narrow particle size distribution. The time required for carbonization is significantly reduced as well. The present study extends the 3D printing to the construction of bubbling reactors with broad applications beyond production of $CaCO_3$.

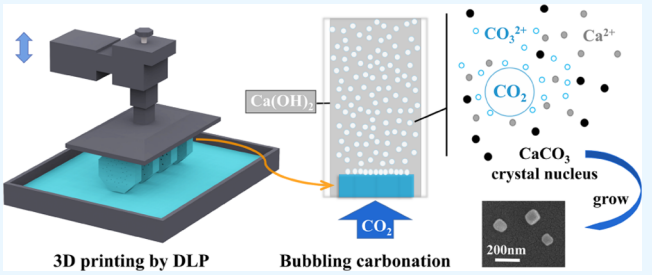

INTRODUCTION

Three-dimensional (3D) printing, also known as additive manufacturing, is a technique for preparing materials or devices with complex or unique three-dimensional structures in a designable way.[1−3] Compared to the traditional manufacturing methods, 3D printing is more flexible in structural design. By changing the design model and the condition of the printer, it is convenient to design and optimize the 3D structure,[4−6] enabling rapid printing and precise manufacturing of a complex device,[7,8] monolith catalyst,[9] and structured reactor.[10] Enhanced fluid flow and heat and mass transfer performances have been achieved by the printed device[11] and catalyst.[12] 3D printing has been employed for the uniform flow rate control of the multistacked microfluidic devices[13] and for the tuning of bubble flow regime in a microfluidized bed.[14]

On the other hand, calcium carbonate is a compound widely found in nature. It has been extensively used as an additive, filler, and pigment material for paper, plastics, rubber, pharmaceuticals, cosmetics, construction materials, animal food, and many others.[15,16] The properties and applications of calcium carbonate are closely related to its morphology, particle size, and crystal structure. For example, vaterite has the potential to be used as a drug carrier[17] or a template for the preparation of a drug carrier.[18] Needle or chain calcium carbonate is widely used in the rubber industry. Submicron spindle-shaped calcium carbonate is an excellent pore-forming agent.[19] Nanosized calcium carbonate with regular morphology, homogeneous crystallinity, and good size distribution is an excellent alternative to some expensive white fillers like white carbon and titanium dioxide.[20] The structure-controllable preparation of calcium carbonate with a narrow particle size distribution is generally required.[21]

Many methods have been applied for the preparation of calcium carbonate. Among them, the intermittent bubbling carbonation is a widely used method in industrial production of calcium carbonate.[22−28] It just needs a simple gas−liquid−solid three-phase reactor with low investment in equipment. The size of CO_2 bubbles[29,30] has a significant effect on the carbonization. The reaction temperature,[22,24] pH,[24] additive,[22,31] and the solution viscosity[24] also have influences. Moreover, the fluid shear caused by vortex and bubble motion can cause abrasion and secondary nucleation of the growing crystals,[32] which in turn affects the morphology and size distribution of the calcium carbonate product. Stirring may break the $CaCO_3$ crystals with the formation of irregular aggregates.[33] The CO_2 injection method and the flow rate of CO_2 significantly also affect the size of the primary calcite particles in a microbubble carbonation reactor.[34,35] These reported studies suggested that the size distribution of CO_2 bubbles has remarkable effects on the size and morphology of the $CaCO_3$ product.

Received: October 22, 2022
Accepted: December 22, 2022
Published: January 6, 2023

https://doi.org/10.1021/acsomega.2c06817
ACS Omega 2023, 8, 2398−2405

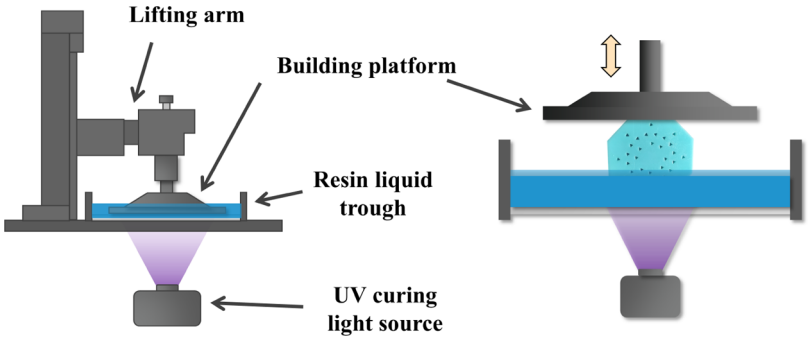

Figure 1. Scheme of the DLP setup.

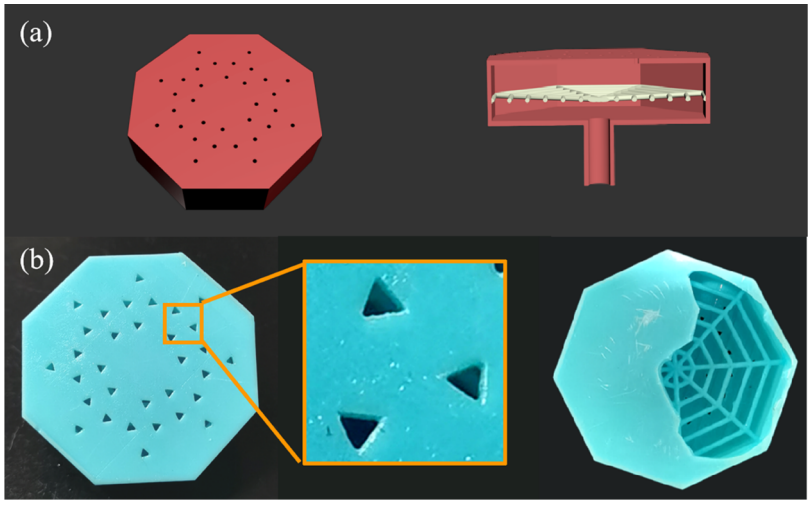

Figure 2. (a) 3D model of the gas distributor with circular gas pores and its internal structure; (b) top view of the gas distributor with triangular gas pores and its internal structure.

In this work, we attempted to optimize the pore size and distribution in a gas distributor by the light-cured 3D printing to tune the bubble distribution and bubble flow regime for the bubbling carbonization without stirring. It was found that the bubble flow regime has a significant effect on the size and morphology of $CaCO_3$ obtained. The homogeneous flow regimes favor the production of calcium carbonate with a uniform morphology and narrow particle size distribution.

2. EXPERIMENTAL SECTION

2.1. Digital Light Processing (DLP). The gas distributor used in this work was printed using a DLP 3D printer (DP-002, Shenzhen Creality 3D Technology Co., Ltd., China). The DLP technique has a high printing efficiency with a high resolution. It can make an individual device of high complexity within several hours. The raw material for this light-cured 3D printing is a kind of photosensitive resin (Shenzhen Creality 3D Technology Co., Ltd., China). Before the model gas distributor was printed, a 3D base model was constructed. Then, the base model was converted into the slice file using a software from the manufacturer of the 3D printer. The slice file was imported into the printer for printing. The parameters such as exposure time and brightness were set for printing. The printed model was subjected to postprocessing with water washing, alcohol washing, and secondary curing to obtain the gas distributor. Figure 1 shows the DLP processing for the printing of the gas distributor. The liquid resin is placed in a liquid tank at the bottom. The lifting arm is lowered according to the programmed settings that the building platform is immersed in the raw material resin. The DLP chip projects the sliced two-dimensional (2D) image of the model onto the building platform, where the resin cures and adheres. After that, the lifting arm rises. The platform moves up one layer distance and continues printing. The process is repeated until the printing is completed.

In this work, the gas distributor was made as an octagonal column with an outer diagonal length of 55.0 mm, a wall thickness of 1.0 mm, an internal height of 12.0 mm, and a bottom connecting tube to introduce carbon dioxide into the gas distributor. The outer diameter of the bottom connecting tube is 6.4 mm with the wall thickness of 1.0 mm. Two kinds of pores (circular and triangular pores) were investigated for the gas distributor. The size of the triangular pore of the gas distributor is expressed as the diameter of the circular pore of the same area. The pore sizes investigated are 0.8, 1.2, and 1.7 mm. Figure 2a shows the top view and the side sectional view of the 3D model of the gas distributor, while Figure 2b shows the images of the gas distributor. A spider web baffle was added into the gas distributor with the optimized position. With the aid of the baffle and the special designed hole distribution, the gas can be distributed as evenly as possible within the distributor.

2.2. Preparation of $CaCO_3$. $CaCO_3$ was prepared by the intermittent bubbling carbonization method. To do so, 4.0 g of $Ca(OH)_2$ (95%, Tianjin Saints Biochemical Technology

https://doi.org/10.1021/acsomega.2c06817
ACS Omega 2023, 8, 2398−2405

Co., Ltd., China) was dispersed in 196.0 g of deionized water under stirring until the suspension was evenly mixed. The $Ca(OH)_2$ suspension was then added to a home-made glass reactor, as shown in Figure 3. Carbon dioxide (99.9%, Tianjin

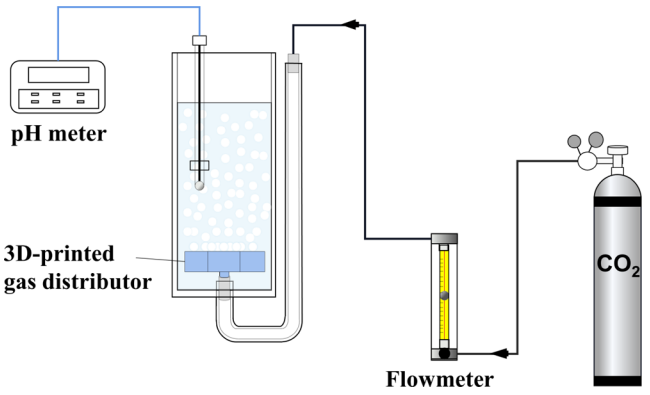

Figure 3. Schematic illustration of the experimental setup for the bubbling carbonization.

Hengtong Gas Co., Ltd., China) was introduced from the bottom of the reactor and carbonized with the calcium hydroxide slurry after passing through the 3D printed distributor. The temperature of the mixture was kept at 25°C. The pH of the mixture was recorded every 15 s with a pH meter, and the carbonation reaction was stopped once the pH dropped below 7.0. After being filtered, washed, and dried (90°C, 12 h), the product was obtained.

Table 1. Average Size of Bubbles for Different Gas Distributors

model	diameter of the pore[a] (mm)	average size of bubbles (mm)
T-1	0.8	4.7
T-2	1.2	5.5
T-3	1.7	7.1

[a]The calculation of the diameter of the pore is explained in Section 2.1.

For the purpose of comparison, the carbonation was also carried out in a stirred reactor (250 mL) without the need for a gas distributor. The stirring speed applied was 500 rpm with the carbon dioxide flow rate of 120 L/h and the reaction temperature of 25 °C.

2.3. Characterization. X-ray powder diffraction (XRD) patterns were recorded using a Rigaku D/max-2500 X-ray diffractometer with a copper target for radiation. The data were collected in the 2θ range of 20−90° with a scan rate of 10°/min and a step size of 0.02°. Based on the half-peak width of the highest peak with $CaCO_3$(104), the average size of the $CaCO_3$ product was calculated using the Scherer equation. Scanning electron microscopy (SEM) images were recorded using a Hitachi Regulus 8100 microscope.

3. RESULTS AND DISCUSSION

3.1. Effects of Gas Flow Rate. As mentioned above, the circular and triangular pores were designed for the gas distributor. Within the experimental conditions investigated, no big difference was found in the $CaCO_3$ produced (Figure S1). Therefore, the subsequent discussions will focus on the use of the triangular pore models with the pore sizes of 0.8, 1.2, and 1.7 mm. These three models were denoted as T-1, T-2, and T-3. The pore size of the distributor affects the size of the bubbles. The larger the pores size, the larger the bubble size. Table 1 exhibits the average size of bubbles with different pore sizes of the gas distributor at the gas flow rate of 90 L/h.

To produce $CaCO_3$ with a uniform morphology and narrow particle size distribution, the gas flow rate has significant effect. It will further affect the bubble distribution, which determines the morphology and particle size distribution of $CaCO_3$ produced. The bubble distribution can be more conveniently described as the bubble flow regime.[14] With the increasing gas flow rate, the bubble flow regime changes from the monodispersed homogeneous regime to the polydispersed homogeneous one and further to the transition bubble regime and finally to the heterogeneous bubble one.[14] Figure 4 illustrates the image of the reaction at the gas flow rate of 90 L/h, with which the monodispersed homogeneous regime appears. Figure S2 shows the images of the bubble distributions at higher gas flow rates with the use of the T-2 gas distributor. When higher gas flow rates (higher than 180 L/h) were applied, coalesced bubbles appears. The bubble flow regime then shifts to the transition bubble regime with a wider bubble size distribution. Finally, when the gas flow rate reaches 280 L/h, the bubble flow system becomes a heterogeneous bubble regime. The gas flow rate higher than 280 L/h was not further investigated in this work because of the nonuniform size distribution of $CaCO_3$ produced with various undesired shapes. The homogeneous regimes favor the production of $CaCO_3$ with a uniform morphology and narrow particle size distribution, as discussed below.

During the reaction, the pH changes of the suspension can be divided into three stages: the slow decline stage, the rapid decline one, and the reaction completion stage. Once pH is

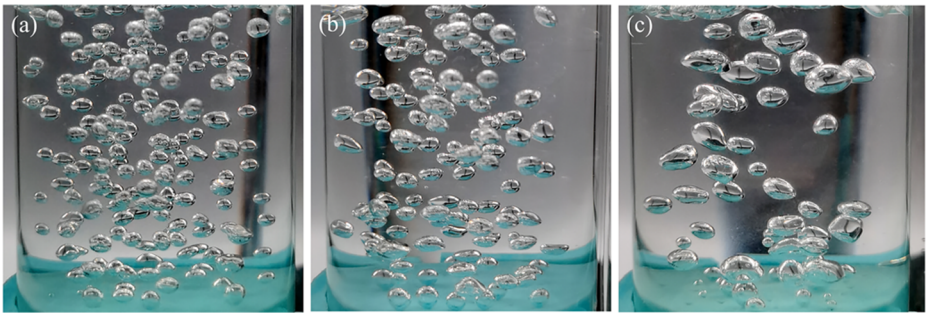

Figure 4. Bubble distribution at 90 L/h with different gas distributors: (a) T-1; (b) T-2; (c) T-3.

https://doi.org/10.1021/acsomega.2c06817
ACS Omega 2023, 8, 2398−2405

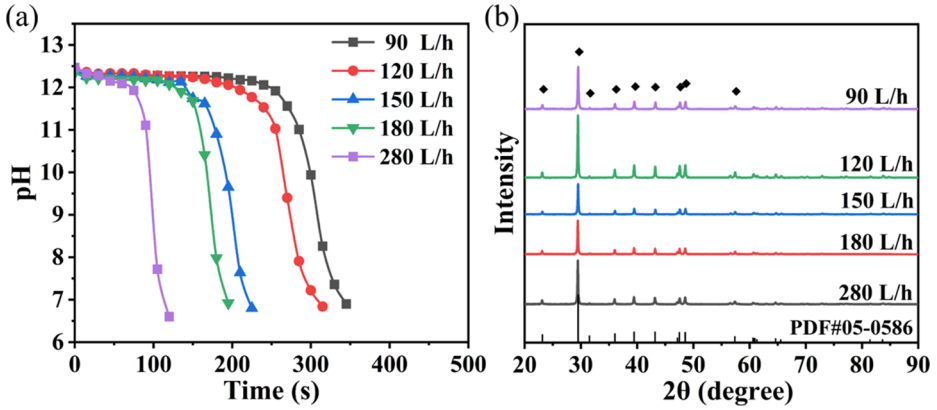

Figure 5. (a) Plot of pH−*t* at different flow rates of CO_2 and (b) X-ray diffraction patterns of the corresponding $CaCO_3$ products. The T-2 gas distributor was applied.

Table 2. Size of $CaCO_3$ under Different CO_2 Flow Rates

flow rate of CO_2 (L/h)	size by XRD analysis (nm)	size by SEM analysis (nm)
90	66.2	68.1
120	63.3	63.9
150	49.8	49.3
180	64.2	63.3
280	71.1	

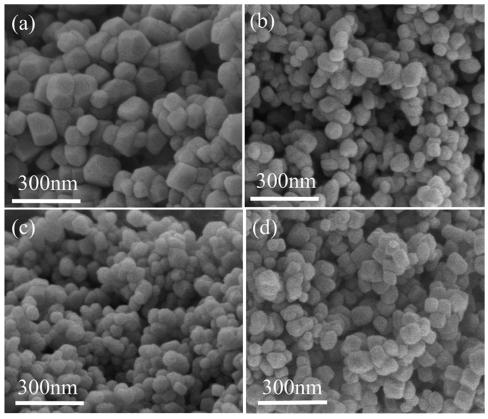

Figure 6. SEM images of $CaCO_3$ products at different flow rates of CO_2: (a) 90 L/h, (b) 120 L/h, (c) 150 L/h, (d) 180 L/h.

below 7.0, the reaction completion phase reaches. After that, the pH value hardly changes anymore. Figure 5a shows the plot of pH with time in the carbonation reaction under different gas flow rates. As the flow rate of the gas increases, the density of bubbles increases with the amount of CO_2 introduced in water. The gas−liquid transfer rate thereby increases with the improvement in the gas−liquid transfer area. The carbonation reaction time becomes shorter, as shown in Figure 5a. Figure 5b exhibits the XRD patterns of the corresponding $CaCO_3$ products. No significant difference in the phase structures of the products can be identified from these patterns. As shown in Table 2, the average size of the $CaCO_3$ product gradually decreases with the increasing flow rate of CO_2 at the range between 90 L/h and 150 L/h, with which homogeneous bubble flow regimes were observed. However, the average size of the $CaCO_3$ product gradually increases when the gas flow rate further increases with the change in the bubble flow regimes. Within the CO_2 flow rates tested, the size of $CaCO_3$ products is less than 71.1 nm.

Figure 6a−d presents SEM images of $CaCO_3$ products at different flow rates of CO_2. The average particle size of the calcium carbonate product was also calculated from the SEM images. The results are close to those obtained from the XRD analyses, as shown in Table 2. At the gas flow rate of 150 L/h, the average particle size of calcium carbonate is the smallest, which is 49.3 nm (Figure 6c). However, when the CO_2 flow rate further increases, the transition bubble regime appears. Larger $CaCO_3$ particles are thus produced with an

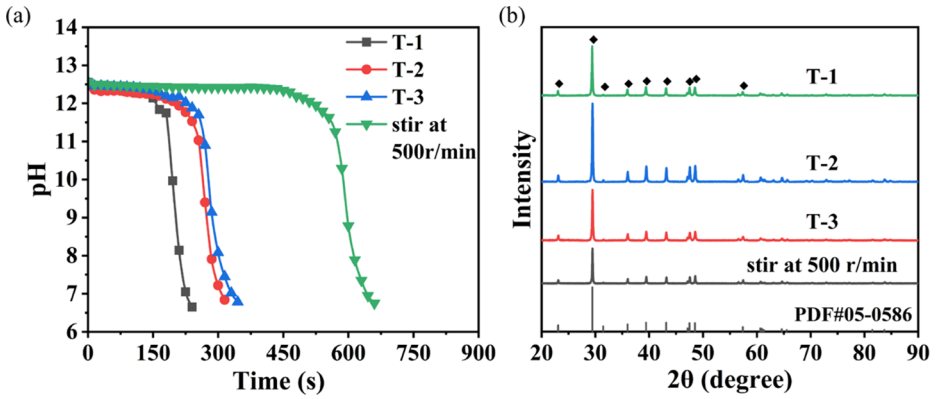

Figure 7. (a) Plot of pH−*t* of carbonization experiments with different gas distributors; (b) XRD patterns of $CaCO_3$ products. The gas flow rate is 120 L/h.

https://doi.org/10.1021/acsomega.2c06817
ACS Omega 2023, 8, 2398−2405

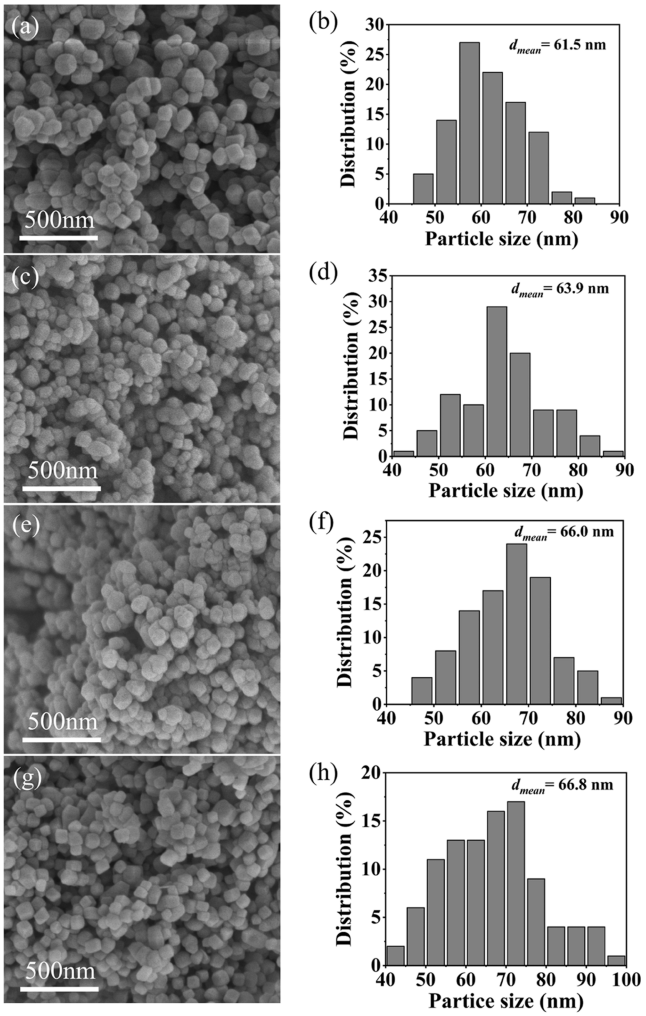

Figure 8. SEM images of $CaCO_3$ products with different gas distributors: (a) T-1; (c) T-2; (e) T-3. Particle size distributions of $CaCO_3$ products with different gas distributors: (b) T-1; (d) T-2; (f) T-3. (g) SEM images of $CaCO_3$ products with external stirring at 500 rpm without a gas distributor and (h) their particle size distribution.

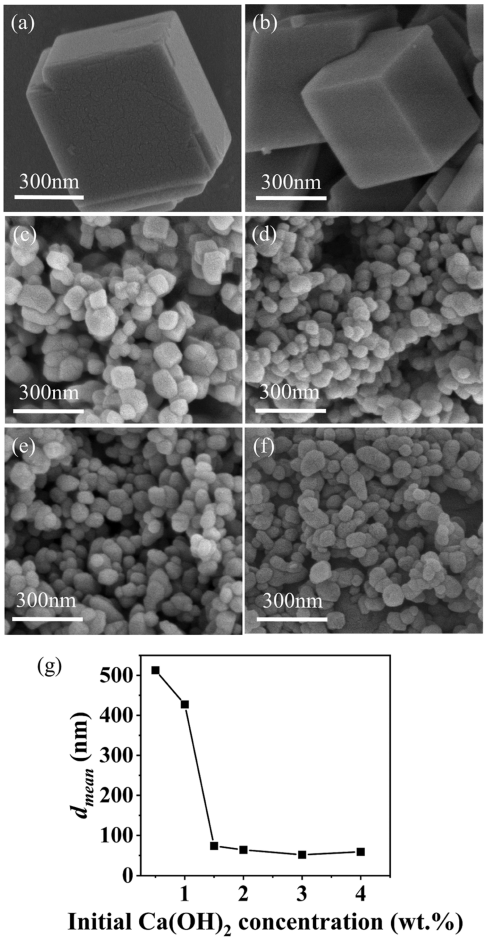

Figure 10. SEM images of $CaCO_3$ products at different initial $Ca(OH)_2$ concentrations: (a) 0.5 wt %; (b) 1 wt %; (c) 1.5 wt %; (d) 2 wt %; (e) 3 wt %; (f) 4 wt %. (g) Effect of the initial $Ca(OH)_2$ concentration on the particle size.

increase in the size difference. However, at the gas flow rate of 280 L/h, polycrystal particles with a size of about 360 nm were formed (Figure S3). The occurrence of polycrystalline particles is associated with the transformation of the bubble flow system into the heterogeneous bubble regime. Hence, to make the $CaCO_3$ with narrow size distribution, the high flow rate of CO_2 is not recommended.

3.2. Effects of the Pore Size of the Gas Distributor.

Figure 7a shows the plot of pH−time in the carbonation reaction with different gas distributors. With the use of 3D printed gas distributors, the bubbles are uniformly dispersed in the liquid phase. This leads to a significant increase in the

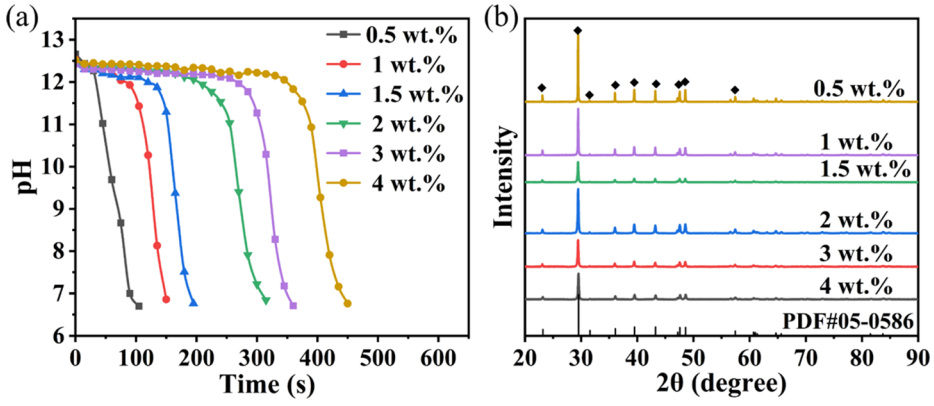

Figure 9. (a) Plots of pH−*t* at different initial $Ca(OH)_2$ concentrations and (b) X-ray diffraction patterns of the corresponding $CaCO_3$ products.

https://doi.org/10.1021/acsomega.2c06817
ACS Omega 2023, 8, 2398−2405

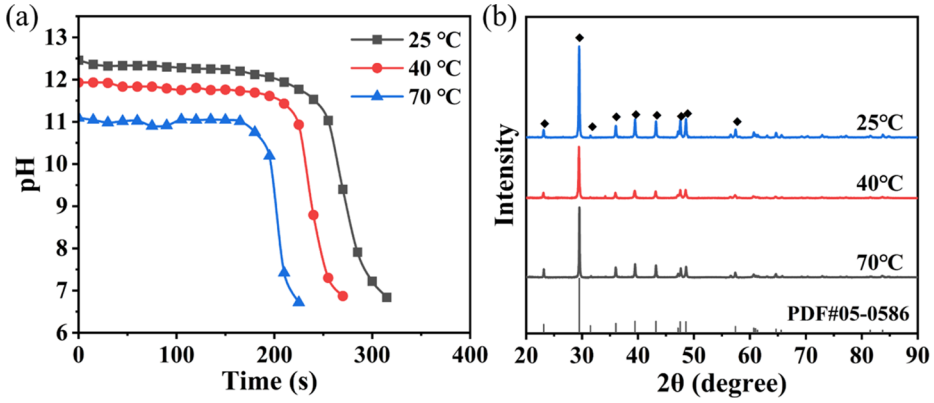

Figure 11. (a) Plots of pH−*t* at different temperatures and (b) X-ray diffraction patterns of the corresponding $CaCO_3$ products.

gas−liquid contact area. The carbonization reaction is thereby accelerated, resulting in a significant reduction in the time required for the carbonization reaction. In comparison, the carbonization reaction time under stirring (500 rpm) without the gas distributor is at least twice longer, as shown in Figure 7a. The time of the carbonation reaction gradually increases as the pore size of the gas distributor increases. As the pore size of the bubbling reactor increases, the size or the volume of the bubbles becomes larger, which reduces the gas−liquid interface area and the residence time of the bubbles.[29,36] This results in the increased time for the carbonation reaction. Figure 7b shows the XRD patterns of $CaCO_3$ products under different conditions. All of the major peaks can be assigned to the calcite phase (PDF #05-0586).

Figure 8a−e shows SEM images of $CaCO_3$ products with particle size distributions from the reactors with gas distributors (T-1, T-2, and T-3). The grain shape appears as roughly cubic and rhombohedral crystals, consistent with the morphological characteristics of calcite crystals by XRD. Meanwhile, the particle sizes from the SEM analyses are consistent with those from the XRD calculations (Table S1). This suggests that the particles of the $CaCO_3$ products obtained using different printed gas distributors are single crystals. The average particle size of $CaCO_3$ gradually increases as the pore size increases, while the shape of the calcium carbonate particles remains essentially unchanged. The product obtained using the gas distributor T-1 has the narrowest particle size distribution with the smallest average particle size of 61.5 nm. In contrast, for the stirred reactor without the 3D printed gas distributor, the calcium carbonate products have a variety of particle shapes with a nonuniform particle size distribution. The average particle size of the products is different from the calculated crystallite size from the XRD analyses (Table S1). Some of the particles are cubic (as shown in Figure 8g,h) with a wide variation in particle size.

3.3. Effect of the Initial $Ca(OH)_2$ Concentration. The carbonization reactions were carried out at different initial concentrations of calcium hydroxide using the T-2 gas distributor. As shown in Figure 9a, the higher the initial concentration of $Ca(OH)_2$, the longer the carbonation reaction time. The XRD patterns (Figure 9b) of $CaCO_3$ products with different initial $Ca(OH)_2$ concentrations indicate that the initial mass concentration of $Ca(OH)_2$ has no effect on the crystal structure of the calcium carbonate products.

Figure 10a−f shows SEM images of $CaCO_3$ products produced at different initial concentrations of $Ca(OH)_2$. As the initial concentration of $Ca(OH)_2$ increases, the average particle size of the calcium carbonate product decreases and the morphology of the particles gradually tends to be spherical. Theoretically, an increase in the initial concentration of $Ca(OH)_2$ will lead to an increase in the supersaturation and viscosity of the solution, which is conducive to increasing the rate of nucleation of $CaCO_3$ particles.[37] This leads to a decrease in the average size of the crystal particles, as shown in Table S1. However, when the initial concentration of $Ca(OH)_2$ is too high, the viscosity of the solution also increases significantly, resulting in a mass transfer obstruction. This increases the chance of bonded growth of nano-calcium carbonate nuclei with high surface energy. The bonded growth of single-crystal particles leads to the irregular shape of calcium carbonate products with a broad particle size distribution.[38]

3.4. Effect of the Carbonization Temperature. Figure 11a shows the relationship between the pH value and the reaction time at different reaction temperatures with the T-2 gas distributor. As the reaction temperature increases, the solubility of calcium hydroxide decreases, leading to a decrease in the initial pH of the solution. At the same time, the higher reaction temperature causes lower viscosity of the mixture. This results in an increase in the crystal growth rate and nucleation rate, leading to a subsequent decrease in the carbonation reaction time. Figure 11b shows the XRD patterns of $CaCO_3$ products at different temperatures, indicating that the change in temperature has no effect on the crystal structure of the calcium carbonate products.

The carbonation reaction is a typical exothermic reaction. Under high temperature conditions, the relative growth rate of each crystal plane changes, leading to an increase in the particle size of the $CaCO_3$ product with a more diverse morphology of the product.[39] As shown in Figure S4, the $CaCO_3$ product gradually changes from a more regular cubic shape to a stalactite, pike, and flower cluster shape in aggregate with increasing temperatures. Therefore, the room temperature reaction is more conducive to the production of regular homogeneous cubic- or rhombohedral-shaped particles.

4. CONCLUSIONS

In this work, the enhanced production of calcium carbonate with a uniform morphology and narrow particle size

https://doi.org/10.1021/acsomega.2c06817
ACS Omega 2023, 8, 2398−2405

distribution has been achieved by the bubbling carbonation reactor with the 3D printed gas distributor. The printed gas distributor can fully ensure that the gas was uniformly dispersed into the liquid phase, causing homogeneous bubble flow regimes. Compared to the stirred reactor, the reactor with the printed distributor possesses higher gas−liquid mass transfer efficiency. The time required for carbonization is thus significantly reduced. The pore size of the gas distributor changes the size and number of bubbles, which in turn affect the bubble distribution. The larger pore size leads to the bigger size of the $CaCO_3$ product. The flow rate of carbon dioxide, on the other hand, has a more significant effect on the flow regime of the bubbles. With the increasing gas flow rate, the bubble flow regime changes from the monodispersed homogeneous to the polydispersed homogeneous regime and further to the transition bubble regime and finally to the heterogeneous bubble regime. To make the $CaCO_3$ product with a uniform size or narrow size distribution, it is necessary to retain the homogeneous bubble regime. An optimized gas flow rate exists, while the high flow rate is not suitable. Moreover, within a certain range, an increase in the initial $Ca(OH)_2$ concentration helps to reduce the particle size of the $CaCO_3$ product. However, the further increasing initial $Ca(OH)_2$ concentration has a negative effect. The experimental studies confirm that the carbonization reaction temperature significantly affects the quality of the $CaCO_3$ product. Only the room temperature reaction favors for production of $CaCO_3$ with the desired uniform morphology. The present work is helpful for the development of novel bubbling reactors beyond the production of $CaCO_3$.

■ ASSOCIATED CONTENT

Supporting Information

The Supporting Information is available free of charge at https://pubs.acs.org/doi/10.1021/acsomega.2c06817.

SEM images of $CaCO_3$ products of gas distributors with different pore shapes; bubble distribution at different flow rates of CO_2; SEM image of $CaCO_3$ products at 280 L/h of CO_2; particle size of $CaCO_3$ under different conditions; SEM image of $CaCO_3$ products at different temperatures (PDF)

■ AUTHOR INFORMATION

Corresponding Author

Chang-jun Liu − *School of Chemical Engineering and Technology, Tianjin University, Tianjin 300350, China; Collaborative Innovation Center of Chemical Science & Engineering, Tianjin University, Tianjin 300072, China;* orcid.org/0000-0001-9918-1638; Email: cjL@tju.edu.cn

Authors

Kai-li Wu − *School of Chemical Engineering and Technology, Tianjin University, Tianjin 300350, China; Collaborative Innovation Center of Chemical Science & Engineering, Tianjin University, Tianjin 300072, China*

Xiang Li − *School of Chemical Engineering and Technology, Tianjin University, Tianjin 300350, China;* orcid.org/0000-0002-5803-2553

Zhong-xing Xu − *School of Chemical Engineering and Technology, Tianjin University, Tianjin 300350, China*

Complete contact information is available at: https://pubs.acs.org/10.1021/acsomega.2c06817

Author Contributions

C.-j.L.: conceptualization, funding acquisition, writing—review & editing, supervision, and project administration. K.-l.W.: writing—original draft, validation, data curation, formal analysis, and investigation. X.L.: investigation. Z.-x.X.: investigation.

Notes

The authors declare no competing financial interest.

■ ACKNOWLEDGMENTS

This work was supported by the National Natural Science Foundation of China (No. 22138009) and the Fundamental Research Funds for the Central Universities of China.

■ REFERENCES

(1) Liu, Z.-X.; Zhou, X.-T.; Liu, C.-J. N-doped porous carbon material prepared via direct ink writing for the removal of methylene blue. *Diamond Relat. Mater.* **2019**, *95*, 121−126.

(2) Cai, Z.-R.; Zhao, S.-D.; Huang, Z.-D.; Li, Z.; Su, M.; Zhang, Z.-Y.; Zhao, Z.-P.; Hu, X.-T.; Wang, Y.-S.; Song, Y.-L. Bubble Architectures for Locally Resonant Acoustic Metamaterials. *Adv. Funct. Mater.* **2019**, *29*, No. 1906984.

(3) Arshavsky-Graham, S.; Anton, E.; Shanny, A.; Janina, B.; Ester, S. 3D-printed microfluidics integrated with optical nanostructured porous aptasensors for protein detection. *Microchim. Acta* **2021**, *188*, 67.

(4) Feng, Y.-R.; Mu, H.-F.; Liu, X.; Huang, Z.-L.; Zhang, H.-M.; Wang, J.-D.; Yang, Y.-R. Leveraging 3D Printing for the Design of High-Performance Venturi Microbubble Generators. *Ind. Eng. Chem. Res.* **2020**, *59*, 8447−8455.

(5) Frey, L. J.; David, V.; Hendrik, O.; Detlev, R.; Jan-Luca, L.; Maximilian, B.; Jan-Hendrik, G.; Gregor, D. W.; Janina, B.; Rainer, K. 3D-printed micro bubble column reactor with integrated microsensors for biotechnological applications: From design to evaluation. *Sci. Rep.* **2021**, *11*, No. 7276.

(6) Zhao, L.-H.-B.; Zeng, G.-F.; Gu, Y.; Tang, Z.-Y.; Wang, G.; Tang, T.; Shan, Y.; Sun, Y.-H. Nature inspired fractal tree-like photobioreactor via 3D printing for CO_2 capture by microaglae. *Chem. Eng. Sci.* **2019**, *193*, 6−14.

(7) Namgung, H.; Kaba, A. M.; Oh, H.; Jeon, H.; Yoon, J.; Lee, H.; Kim, D. Quantitative Determination of 3D-Printing and Surface-Treatment Conditions for Direct-Printed Microfluidic Devices. *BioChip J.* **2022**, *16*, 82−98.

(8) Feng, Y.-R.; Zhang, H.-M.; Wang, J.-D.; Yang, Y.-R. Performance Evaluation and Scale-Up Behavior of an Engineered In-Line Mixer for 3D Printing. *Ind. Eng. Chem. Res.* **2021**, *60*, 11568−11578.

(9) Zhu, J.; Wu, P.-W.; Chao, Y.-H.; Yu, J.-T.; Zhu, W.-S.; Liu, Z.-C.; Xu, C.-M. Recent advances in 3D printing for catalytic applications. *Chem. Eng. J.* **2022**, *433*, No. 134341.

(10) Hock, S.; Marcus, R. 3D-Structured Monoliths of Nanoporous Polymers by Additive Manufacturing. *Chem. Ing. Tech.* **2020**, *92*, 525−531.

(11) Reitze, A.; Marcus, G.; Julia, R. Characterization of Liquid-Phase Distribution in 3D Printed Structured Packings with an Enclosed Column Wall. *Ind. Eng. Chem. Res.* **2022**, *61*, 740−746.

(12) Miriam, G.-C.; Francisco, B.-M.; Juan, C. N. D. M.; Kamal, U. M. M.; Fátima, A.-T.; Ralf, O.; Jose, A. O.; Walther, B.; Andreas, H.; Achim, W.; Harvey, A.-G. 3D-printed structured catalysts for CO_2 methanation reaction: Advancing of gyroid-based geometries. *Energy Convers. Manage.* **2022**, *258*, No. 115464.

(13) Park, Y.-J.; Taejong, Y.; Se-Jun, Y.; Donghyun, Y.; Dong-Pyo, K. A 3D-printed flow distributor with uniform flow rate control for multi-stacked microfluidic systems. *Lab Chip* **2018**, *18*, 1250−1258.

(14) Zhang, Y.; Kheng-Lim, G.; Yuen-Ling, N.; Yvonne, C.; Vladimir, Z. Design and Investigation of a 3D-Printed Micro-Fluidized Bed. *ChemEngineering* **2021**, *5*, 62.
(15) Kuo, D.; Tatsuya, N.; Satoshi, K.; Takashi, K. Bioinspired Environmentally Friendly Amorphous CaCO3-Based Transparent Composites Comprising Cellulose Nanofibers. *ACS Omega* **2018**, *3*, 12722−12729.
(16) Zhang, H.; Zeng, X.-F.; Gao, Y.-F.; Shi, F.; Zhang, P.-Y.; Chen, J.-F. A Facile Method To Prepare Superhydrophobic Coatings by Calcium Carbonate. *Ind. Eng. Chem. Res.* **2011**, *50*, 3089−3094.
(17) Fujiwara, M.; Kumi, S.; Kenichi, M.; Ying-chun, Z.; Yoshiko, N. Calcium carbonate microcapsules encapsulating biomacromolecules. *Chem. Eng. J.* **2008**, *137*, 14−22.
(18) Wang, A.; Yang, Y.; Qi, Y.-F.; Qi, W.; Fei, J.-B.; Ma, H.-C.; Zhao, J.; Cui, W.; Li, J.-B. Fabrication of Mesoporous Silica Nanoparticle with Well-Defined Multicompartment Structure as Efficient Drug Carrier for Cancer Therapy in Vitro and in Vivo. *ACS Appl. Mater. Interfaces* **2016**, *8*, 8900−8907.
(19) Xie, Y.-J.; Pan, Y.-F.; Cai, P.-X. Novel PVA-Based Porous Separators Prepared via Freeze-Drying for Enhancing Performance of Lithium-Ion Batteries. *Ind. Eng. Chem. Res.* **2020**, *59*, 15242−15254.
(20) Karakaş, F.; Behzad Vaziri, H.; Mehmet, S. Ç. Effect of precipitated calcium carbonate additions on waterborne paints at different pigment volume concentrations. *Prog. Org. Coat.* **2015**, *83*, 64−70.
(21) Cheng, B.; Lei, M.; Yu, J.-G.; Zhao, X.-J. Preparation of monodispersed cubic calcium carbonate particles via precipitation reaction. *Mater. Lett.* **2004**, *58*, 1565−1570.
(22) Yash, B.; Vishnu, K. P.; Jian, L. Synthesis of micro and nano-sized calcium carbonate particles and their applications. *J. Mater. Chem. A* **2014**, *2*, 14270−14288.
(23) Xiang, L.; Xiang, Y.; Wang, Z. G.; Jin, Y. Influence of chemical additives on the formation of super-fine calcium carbonate. *Powder Technol.* **2002**, *126*, 129−133.
(24) Tan, W. L.; Ahmed, A. L.; Leo, C. P.; Lam, S. S. A critical review to bridge the gaps between carbon capture, storage and use of $CaCO_3$. *J. CO2 Util.* **2020**, *42*, No. 101333.
(25) Burns, J. R.; JJ, J. Monitoring of $CaCO_3$ production on a spinning disc reactor using conductivity measurements. *AIChE J.* **2005**, *51*, 1497−1507.
(26) Liang, Y.; Chu, G.-W.; Wang, J.-X.; Huang, Y.; Chen, J.-F.; Sun, B.-C.; Shao, L. Controllable preparation of nano-$CaCO_3$ in a microporous tube-in-tube microchannel reactor. *Chem. Eng. Process.: Process Intensif.* **2014**, *79*, 34−39.
(27) Du, L.; Wang, Y.-J.; Luo, G.-S. In situ preparation of hydrophobic $CaCO_3$ nanoparticles in a gas−liquid microdispersion process. *Particuology* **2013**, *11*, 421−427.
(28) Freddy, L.; Mara, A.; Fabio A, D.; Samir, B. Factors controlling and influencing polymorphism, morphology and size of calcium carbonate synthesized through the carbonation route: A review. *Powder Technol.* **2022**, *398*, No. 117050.
(29) Grimes, C. J.; Thomas, H.; Mohamed S, M.; Tariq, M.; David W, Y. Calcium Carbonate Particle Formation through Precipitation in a Stagnant Bubble and a Bubble Column Reactor. *Cryst. Growth Des.* **2020**, *20*, 5572−5582.
(30) Liendo, F.; Mara, A.; Fabio, A. D.; Samir, B. Optimization of $CaCO_3$ synthesis through the carbonation route in a packed bed reactor. *Powder Technol.* **2021**, *377*, 868−881.
(31) Zheng, T.-W.; Yi, H.-H. Formation and Stabilization of Vaterite Aggregate Grooves with Aspartic Acid (Asp) by Bubbling CO_2 into a $Ca(OH)_2$ Suspension. *Cryst. Res. Technol.* **2021**, *56*, No. 2100136.
(32) Tsutsumi, A.; Jenn, Y. N.; Liang, S. F. Role of the bubble wake in fine particle production of calcium carbonate in bubble column systems. *Ind. Eng. Chem. Res.* **1991**, *30*, 2328−2333.
(33) Feng, Z.-Q.; Yang, T.-Y.; Dong, S.-C.; Wu, T.; Jin, W.; Wu, Z.-Y.; Wang, B.-P.; Liang, T.-T.; Cao, L.; Yu, L. Industrially synthesized biosafe vaterite hollow $CaCO_3$ for controllable delivery of anticancer drugs. *Mater. Today Chem.* **2022**, *24*, No. 100917.
(34) Bang, J.-H.; Young Nam, J.; Wonbaek, K.; Kyung Sun, S.; Chi Wan, J.; Soo Chun, C.; Seung-Woo, L.; So-Jin, P.; Myung Gyu, L. Specific surface area and particle size of calcium carbonate precipitated by carbon dioxide microbubbles. *Chem. Eng. J.* **2012**, *198*, 254−260.
(35) Wang, K.; Wang, Y. J.; Chen, G. G.; Luo, G. S.; Wang, J. D. Enhancement of mixing and mass transfer performance with a microstructure minireactor for controllable preparation of $CaCO_3$ nanoparticles. *Ind. Eng. Chem. Res.* **2007**, *46*, 6092−6098.
(36) Li, X.; Wang, W.; Zhang, P.; Li, J.; Chen, G. Interactions between gas-liquid mass transfer and bubble behaviours. *R. Soc. Open Sci.* **2019**, *6*, No. 190136.
(37) Wen, Y.; Xiang, L.; Jin, Y. Synthesis of plate-like calcium carbonate via carbonation route. *Mater. Lett.* **2003**, *57*, 2565−2571.
(38) Gómez-Díaz, D.; José M, N.; Begoña, S. Analysis of mass transfer in the precipitation process of calcium carbonate using a gas/liquid reaction. *Chem. Eng. J.* **2006**, *116*, 203−209.
(39) Chang, R.; Dasol, C.; Min Hee, K.; Youngjune, P. Tuning Crystal Polymorphisms and Structural Investigation of Precipitated Calcium Carbonates for CO_2 Mineralization. *ACS Sustainable Chem. Eng.* **2016**, *5*, 1659−1667.

https://doi.org/10.1021/acsomega.2c06817
ACS Omega 2023, 8, 2398−2405